Selectivity and competition between the anodic evolution of oxygen and chlorine

Vos, J.G.

Citation

Vos, J. G. (2019, December 4). *Selectivity and competition between the anodic evolution of oxygen and chlorine*. Retrieved from https://hdl.handle.net/1887/81383

Author: Vos, J.G.
Title: Selectivity and competition between the anodic evolution of oxygen and chlorine
Issue Date: 2019-12-04

3

SELECTIVITY TRENDS BETWEEN OXYGEN EVOLUTION AND CHLORINE EVOLUTION ON IRIDIUM-BASED DOUBLE PEROVSKITE

Optimization of the selectivity between oxygen evolution and chlorine evolution is highly desired for several energy-intensive electrochemical processes, but the strong correlation between occurrence of the two reactions prevents a straight-forward approach of doing so. In this chapter, we look deeper into this correlation by studying the selectivity and interdependence of the OER and CER on a series of iridium-based double perovskites, which are materials that have shown high OER activity and may be usable in acidic electrolyzers. For all studied catalysts, we found a strong linear correlation between CER and OER activity, as well as comparable selectivity, strengthening the long-proposed notion that a scaling relationship exists between the two reactions. We also employed online inductively coupled plasma mass spectrometry (ICP-MS) measurements to probe the material stability and how this is affected by chloride. We found that chloride selectively enhances the dissolution of the noble metal component. A reaction order analysis was performed to gain insight in the CER mechanism, the effect of surface area changes due to adventitious leaching, and the observed suppressing effect of chloride on the OER.

THIS CHAPTER IS BASED ON THE FOLLOWING PUBLICATION:

Vos, J. G.; Liu, Z.; Speck, F. D.; Perini, N.; Fu, W.; Cherevko, S.; Koper, M. T. M. Selectivity Trends Between Oxygen Evolution and Chlorine Evolution on Iridium-Based Double Perovskites in Acidic Media. ACS Catal. 2019, 9 (2), 8561–8574.

3.1. Introduction

Proton Exchange Membrane (PEM) electrolyzers, which currently offer the best performance for water splitting on the industrial scale, generally employ acidic pH. Ir is the only material known to retain long-term stability under acidic OER operation, either as a pure oxide or as a dopant. Virtually no acidic OER anode is known that does not rely on Ir.[152] Unfortunately, the scarcity of Ir is a crippling limitation to large-scale implementation of PEM electrolyzers, and a large body of research has been devoted to reducing the needed Ir loading, such as by increasing the catalyst active surface area, or developing Ir-based materials with higher intrinsic activity. A recent example of Ir-based materials with lower intrinsic Ir mass loading are Ir-based double perovskites, which offer a way to reduce the amount of Ir needed while retaining the high catalytic OER performance.[153] Previous work by some of us showed that the high OER performance of these materials is related to their surface instability in acid, leading to amorphization of the surface and formation of a highly active surface layer.[154] An interesting question is how these Ir-based double perovskites perform as CER electrocatalysts, and how parallel CER impacts their stability. They represent an attractive system of study also because of the possibility of studying a series of closely related structures. The Ir double perovskite structure is represented by A_2BIrO_6 and allows a degree of freedom in the type of A and B cations, meaning that many different perovskites can be prepared.

In this chapter, we explore parallel evolution of oxygen and chlorine on a series of double perovskites and investigate their selectivity and stability, as well as the interdependence between the two reactions in acidic media of pH ~ 1. We applied the RRDE method and scanning protocol described in Chapter 2 to measure the OER and CER on GC-supported, dropcasted double perovskite microparticles. Similar to Chapter 2, relatively low chloride concentrations ($0 < [Cl^-] < 120$ mM) were chosen to study the CER, since the competition between the OER and CER is the most prevalent under these conditions. The double perovskites used can be written as Ba_2BIrO_6, where B = Pr, Nd, La, Sn, Y, Tb, and Ce. The material Sr_2YIrO_6 was also included with the aim to vary the A cation. Commercial IrO_2 was included as reference material.

3.2. Experimental

3.2.1. Chemicals

$HClO_4$ (60%) and NaCl (EMSURE/Analysis grade) were purchased from Merck. Ir-based double perovskites were synthesized as reported previously.[153] IrO_2 nanoparticles (Premion, 99.99%) were purchased from Alfa-Aesar. All purchased chemicals were used as received. The water used for all experiments was prepared by a Merck Millipore Milli-Q system (resistivity 18.2 MΩcm, TOC < 5 p.p.b.).

3.2.2. Synthesis of the double perovskites and X-ray powder diffraction

Samples of A_2BIrO_6 (A = Ba and Sr; B = Lanthanides, Y and Sn) were prepared from $BaCO_3$, $SrCO_3$, La_2O_3, CeO_2, Pr_6O_{11}, Nd_2O_3, Tb_4O_7, Y_2O_3, SnO_2 and Ir metal using methods based on standard solid-state reactions.[155,156] The La_2O_3 and Nd_2O_3 powders were preheated at 950 °C overnight before use. The well-ground mixtures were placed in alumina crucibles and allowed to react at 800 °C overnight. The resultant powders were then sintered at 1250 °C for two days with intermittent regrinding, and, finally, the samples were furnace cooled to room temperature. Every synthesis was carried out in air.

X-ray powder diffraction patterns were collected on a Philips X'Pert diffractometer in Bragg-Brentano geometry, equipped with a X'Celerator detector and a Cu-Kα source. Diffraction patterns were collected in steps of $2\theta = 0.020°$, with a 10 s counting time per step in the range $15° < 2\theta < 90°$.

3.2.3. Online electrochemical ICP-MS analysis

Investigations of the chloride impact on the stability of iridium based double perovskites were performed using an electrochemical scanning flow cell (SFC) with online inductively coupled plasma mass spectrometry (ICP-MS) analysis to detect dissolution products in direct correlation to potential and current density. The SFC is a small polycarbonate cell with an electrolyte flow of 192 $\mu L\ min^{-1}$ able to perform classical three electrode electrochemical experiments. The cell's inlet is connected to a counter electrode compartment, housing a graphite rod (Sigma Aldrich, 99.995%), while a Ag/AgCl reference electrode (Metrohm) is connected by a separate channel directly to the working electrode. The reference electrode was calibrated vs. the RHE, against which all potentials are reported. The working electrode can be moved with an xyz-stage (Physik Instrumente, M-403), which allows fast screening of multiple catalyst spots on a 5x5 cm glassy carbon plate (HTW, SIGRADUR® G, 5×5 cm). The outlet of the SFC is connected to the ICP-MS (Perkin Elmer, NexION 350x) to detect dissolution products. The ICP-MS was calibrated for the elements A, B and Ir with a four-point calibration slope by adding specific amounts of standard solutions (Merck, Certipur®, Ir, Pr, Y, Ba, Sr) to the electrolyte. More details about the online SFC ICP-MS system can be found in previous publications.[157–159] The SFC was operated using 0.1 M $HClO_4$ (Merck, Suprapur®) as an electrolyte in control experiments, and addition of 50 mM NaCl (Sigma Aldrich, 99.5%) provided information of chloride impact on the stability. Catalysts were dropcasted from water based suspensions containing 0.27 mg(Ir)/mL and 20 µL of Nafion (Sigma Aldrich, 5wt.% in aliphatic alcohols). Using 0.3 µL of those suspensions for dropcasting resulted in dried catalyst spots whose sizes (see Table A 9.3.1) were measured using a Keyence Laser Profilometer (VK-X200 series). Surface area normalization was based on these spot sizes. Each measurement was carried out in duplo to ensure reproducibility. Data from single measurements are reported.

3.2.4. General electrochemical procedures

All experiments were carried out at room temperature (~20 °C).

The electrochemical experiments were done using home-made two-compartment borosilicate glass cells with solution volumes of 100 mL. Before first-time use, all glassware was thoroughly cleaned by boiling in a 3:1 mixture of concentrated H_2SO_4 and HNO_3. When not in use, all glassware was stored in a 0.5 M H_2SO_4 solution containing 1 g/L $KMnO_4$. Before each experiment, glassware was thoroughly rinsed with water, and then submerged in a dilute (~0.01 M) solution of H_2SO_4 and H_2O_2 to remove all traces of $KMnO_4$ and MnO_2. The glassware was then rinsed three times with water and boiled in water. The rinsing-boiling procedure was repeated two more times.

An IviumStat potentiostat (Ivium Technologies) was used during electrochemistry experiments. All experiments except voltammetric characterizations were 85% iR-compensated in-situ. The solution resistance was measured with electrochemical impedance spectroscopy at 0.75 V vs. RHE, by observing the absolute impedance in the high frequency domain (100-50 KHz) corresponding to a zero-degree phase angle.

3.2.5. Rotating ring-disk electrode (RRDE) procedures

RRDE experiments were performed in 0.1 M $HClO_4$ solutions with a pH value of 1.20 ± 0.05, as measured with a Lab 855 meter equipped with a glass electrode (SI Analytics). The solutions were saturated with Ar (Linde, purity 6.0) before experiments. Solutions were bubbled with Ar gas during forced convection experiments, Ar was used to blanket the solution in stationary conditions. The reference electrode was a HydroFlex® reversible hydrogen electrode (Gaskatel), separated from the main solution using a Luggin capillary, to fix the reference sensing point and to prevent mixed potentials at the reference due to dissolved Cl_2 gas. The Luggin tip was distanced ~2 cm from the working electrode, to minimize distortion of the current distribution across the electrode surface,[116] and it was aligned to the center of the working electrode, to minimize electrical cross-talk.[137,138] All potentials in this chapter are reported on the RHE scale. A Pt mesh was used as counter electrode, separated from the main solution with a coarse sintered glass frit.

RRDE measurements were done with an MSR rotator and E6 ChangeDisk RRDE tips in a PEEK shroud (Pine Research). GC disks (Pine Research Instrumentation, surface area 0.196 cm^2) were prepared to a mirror finish by hand polishing on Microcloth pads with diamond paste suspensions down to 0.05 μm particle size (Buehler), followed by rinsing and sonication of the electrode in water for 3 minutes. The fine-ground catalyst powders were prepared as suspensions of 3 mg/mL (total catalyst mass) in EtOH (AR/Analysis grade, Acros organics). After drying the prepared GC surface with compressed air, the RRDE tip was placed upside down in the MSR rotator. Thin films of catalyst were prepared by dropcasting 2.5 μL well-stirred EtOH suspension (formal loading ~38 $\mu g * cm^{-2}$, total catalyst mass) onto the GC surface, followed by drying under rotation at 175 RPM. After the solvent had visibly evaporated, the surface was further dried with hot air for several minutes.

Before any RRDE experiment, the Pt ring was electrochemically reactivated by scanning from -0.1 V to 1.7 V at 500 mV s^{-1} for 20 scans at 1500 RPM. Hydrodynamic experiments were done at 1500 RPM by scanning the disk electrode in the range of 1.3 – 1.55 V at 10 mV s^{-1}. In between experiments, the disk electrode was kept at 1.3 V. Ring currents were corrected for constant background currents and product collection delay. The latter arises from the time needed for products formed on the disk to reach the ring, and was approximately 200 ms at 1500 RPM.

The liquid phase collection factor of the ring-disk system, N_l, was determined by studying the $\mathrm{Fe[CN]_6^{3-}/Fe[CN]_6^{4-}}$ redox couple in a solution of 10 mM $\mathrm{K_3Fe[CN]_6}$ and 0.1 M $\mathrm{KNO_3}$, using the Pt ring with a freshly prepared blank GC electrode. The value was 0.241 within 5% accuracy. The collection factor for dissolved $\mathrm{Cl_2}$ was also measured in the same setup, by evolving chlorine selectively on $\mathrm{Ba_2PrIrO_6}$ in 0.1 M $\mathrm{HClO_4}$ + 0.1 M NaCl at a potential of 1.48 V vs. RHE, right before the kinetic onset of OER. The collection factor for dissolved chlorine, N_{Cl_2}, was found to be 0.215 within 3% accuracy, slightly lower than N_l. The difference can be attributed to the higher solution pH compared to the work in Chapter 2, which causes an increase in the degree of $\mathrm{Cl_2}$ dissociation into $\mathrm{Cl^-}$ and HClO, the latter of which is not detectable using present methods (see section 2.3.1). The value for N_{Cl_2} was used in all calculations concerning OER and CER current separation.

3.2.6. Parallel OER and CER – Activity measurements

Before initiating quantitative measurements, the GC-supported thin films were scanned 20 times in chloride-free 0.1 M $\mathrm{HClO_4}$ between 1.3 – 1.55 V, into the OER region, at 1500 RPM. This was done to ensure unchanging catalyst behavior during experiments. The Pt ring was initially deactivated. The final scan of this procedure was taken as the data for 'pure' OER activity. In the next step, the double layer capacitance was determined to allow a degree of normalization of the currents vs. electrochemical surface area (see below). Finally, 20 mM NaCl was added to the solution, and the GC supported thin film was scanned once again between 1.3 – 1.55 V at 1500 RPM, with the Pt ring fixed at 0.95 V vs. RHE for $\mathrm{Cl_2}$ detection. These three steps were performed strictly sequentially using the same film and setup. The procedure of steps was repeated for each catalyst material at least three times, in independently prepared solutions and glassware, and using freshly prepared electrode films.

Measurement of the double layer capacitance $(C_{dl})_E$ was done by scanning the electrode in the potential window of 0.05 – 0.15 V at scan rates of 25, 50, 75 and 100 mV/s (see Figure A 9.3.7). The value of the double layer capacitance $(C_{dl})_E$ was calculated from the slope of the charging current around 0.1 V vs. scan rate, $i_{(C_{dl})_{0.1V}} = (C_{dl})_{0.1V} * \nu$ (see Figure A 9.3.8). From $(C_{dl})_{0.1V}$, the electrochemical surface area could be approximated for each individual experiment by normalizing the activity to the specific capacitance of the double layer, assuming 0.059 mF cm^{-2} for the latter.[66] Reported values for each type of catalyst are averaged from individually normalized activities.

3.2.7. Parallel OER and CER – CER selectivity vs. [Cl-] measurements

Just like the activity measurements, the GC-supported thin films were scanned at least 20 times in chloride-free 0.1 M $\mathrm{HClO_4}$ between 1.3 – 1.55 V at 1500 RPM, to ensure unchanging catalyst behavior during experiments. Following this, the ring was activated and kept at 0.95 V vs. RHE during all measurements. The electrode was then again scanned between 1.3 – 1.55

V at 1500 RPM, while increasing the concentration of NaCl in steps from 0 mM to 120 mM. No attempt at normalization versus surface area was undertaken for these experiments, since we were interested in OER vs. CER selectivity and their reaction orders only, which are not affected by current normalization. Details about the preparation of the amorphous, hydrated IrO_x/GC catalyst can be found in section 9.1.2.

3.3. Results and discussion

3.3.1. ICP-MS measurements and effect of chloride on stability

A series of Ba_2BIrO_6 compounds (B = Pr, Nd, La, Sn, Y, Tb, Ce) and Sr_2YIrO_6 were synthesized and investigated for OER and CER activity and selectivity. We first investigated the stability of these materials under representative electrochemical conditions, since it has recently been shown that Ir-based perovskites are unstable in acidic media. Ba_2PrIrO_6[153,154] and the single perovskite $SrIrO_3$[160] tend to leach out both Ir and non-noble metals from their lattice during sustained oxygen evolution, leading to an amorphous IrO_x outer surface layer that is highly active towards the OER, expectedly more so than the bulk material. The main driver for this instability appears to be the favorable thermodynamics of non-noble metal dissolution in acidic media, followed by co-dissolution and/or collapse of the interspaced IrO_6 octahedra. Since our experiments involve CER in addition to the OER, it was necessary to study the effect of chloride on the leaching behavior of the studied materials.

We performed online electrochemical ICP-MS measurements to follow the dissolution of Ir and the A + B cations under electrochemical conditions in 0.1 M $HClO_4$, in presence and absence of 50 mM NaCl. Each experiment was comprised of the same electrochemical protocol seen in Figure 3.1A (top). Contact was made at 0.05 V, while subsequent potential cycling at 200 mV s^{-1} to 1.6 V was used to reach reproducible CVs. After a “resting” period at 1.2 V in which the dissolution subsided to its background signal, a linear sweep voltammogram (LSV) at 10 mV s^{-1} to 1.65 V, along with the integral of Ir dissolution, was used to calculate the stability number (*S-number*).[154] In the presence of chlorides, the formula for calculating the S-number was adapted according to Eq. A 9.3.3 to include the formation of chlorine gas. Ba_2PrIrO_6, Ba_2YIrO_6, Sr_2YIrO_6 and Ba_2CeIrO_6 were chosen as representative double perovskites.

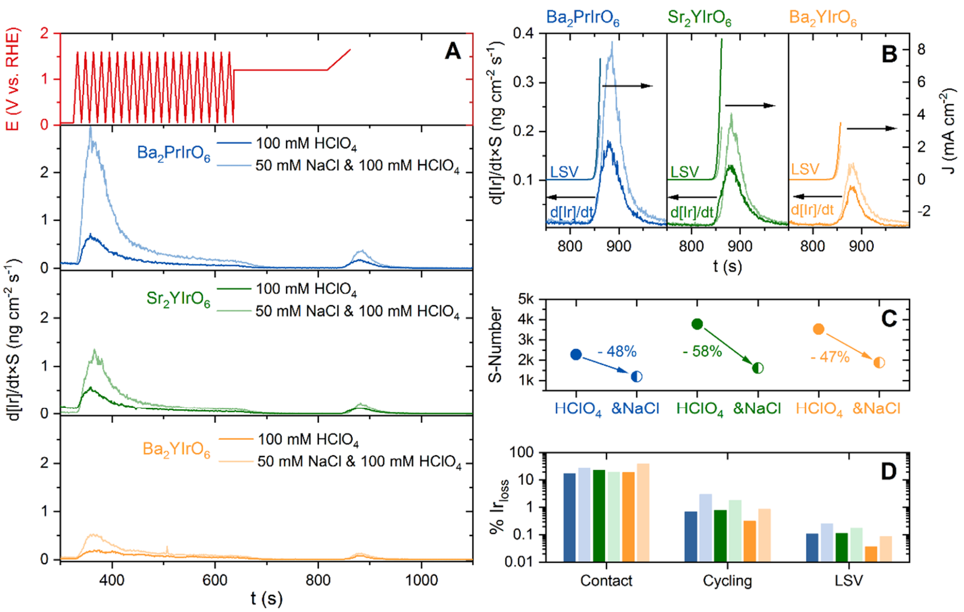

Figure 3.1: Online electrochemical iridium dissolution from ICP-MS measurements. Panel A: Ir dissolution over time correlated with the applied E vs. t protocol (red) for Ba_2PrIrO_6 (blue), Sr_2YIrO_6 (green), and Ba_2YIrO_6 (yellow), in 0.1 M $HClO_4$ (solid) and 0.1 M $HClO_4$ with 50 mM NaCl (pale). For clarity reasons, the initial contact peak is not shown (see Figure A 9.3.1 for the full version). Panel B: Ir dissolution along with the current density of the LSV of the E vs. t protocol. Panel C: S-number (amount of gases evolved per amount of Ir dissolved) comparison in presence and absence of 50 mM NaCl. Panel D: Total dissolved amount of Ir during initial contact with the electrolyte, cycling and the LSV, as determined from the initial spot loading (see also Table A 9.3.1).

Figure 3.1 summarizes online ICP-MS Ir dissolution from Ba_2PrIrO_6, Ba_2YIrO_6 and Sr_2YIrO_6 during the electrochemical protocol. Additional dissolution data for Ba_2CeIrO_6 is shown in the SI. Similar to a previous report,[154] all materials experience major Ir leaching immediately upon contact with the acidic electrolyte (Figure 3.1D), during which the electrode is conditioned at 0.05 V vs. RHE. Cycling of the electrode promotes the rate of iridium leaching, suggesting that the effect is strongly dependent on transient changes in the catalyst matrix.[82] Non-noble components (Ba, Pr, Sr, Y and Ce) however show little to no potential dependent dissolution and merely dissolve upon electrolyte contact. Table A 9.3.2 offers an overview of all integrated dissolution rates. In this table, Ba_2PrIrO_6 in chloride-free electrolyte shows enhanced contact dissolution rates of Ba compared to Pr and Ir. This conforms to previously reported XPS data on Ba_2PrIrO_6 which was exposed to a similar environment.[153] Interestingly, Sr in Sr_2YIrO_6 shows a small but more pronounced potential dependent dissolution during cycling than Ba in Ba_2PrIrO_6 and Ba_2YIrO_6. A lack of a clear trend for the total dissolution of any element in the presence of chloride is due to the big percentage of the contact dissolution on the overall dissolved amount (90-100%). The contact peak is rarely reproducible for the same catalyst as it depends on many factors. We therefore limit the following discussion to the dissolution observed during potentiodynamic control. Most importantly, the dissolution of Ir is increased significantly during both the cycling and the linear potential ramp (Figure 1D). To look into this aspect in more detail, the extent of Ir leaching was correlated with the catalytic current in the voltammogram during the final LSV (Figure 1B). This allowed the calculation of the S-numbers for both the pure OER in $HClO_4$, as well as a competitive oxygen and chlorine evolution in the presence of chloride (Figure 3.1C). A faradaic efficiency of 100% towards the OER, and 90% chlorine evolution to 10% oxygen was assumed according to RRDE experiments, respectively (see section 3.2.7). The stability number *S* (plotted in Figure 3.1C) had a very similar value for Ba_2PrIrO_6, Ba_2YIrO_6 and Sr_2YIrO_6. For Ba_2CeIrO_6, OER activity and Ir dissolution during the linear sweep were too low to accurately measure, and *S* could not be determined. In presence of chloride, all materials experience more Ir dissolution, as illustrated by a roughly 50% decrease in *S*, which is in line with previous results on the stability of noble metals such as Pt and Rh in presence of chloride.[90] These results suggest that the dissolution of noble metal centers is impacted very differently during CER than during the OER. We speculate that whereas during the OER, the dissolution is driven by formation of higher oxide species, Cl^- may enhance Ir dissolution specifically by forming chloro-iridate complexes such as $IrCl_3$ and $Ir[Cl]_6^{3-}$. We note that the total amount of Ir that dissolved from the double perovskites during these experiments is several orders of magnitude larger than what has been reported for IrO_2.[161] This means that IrO_2 represents an interesting, transiently stable material for comparison in this study.

3.3.2. Catalyst characterization

To verify the bulk properties of the materials tested in this study, powder XRD patterns were measured (Figure A 9.3.2). The patterns generally agree with those reported in the literature;[155,156,162] in particular, the presence of the super lattice lines at about 18° and 35°, which in the double cubic cell are indexed as (111) and (311) respectively, suggest an ordered arrangement of the BO_6 and IrO_6 octahedra. The IrO_2 shows poor crystallinity, displaying a single broad peak of overlapping rutile (110) and (101) reflections around 28° and 35°, as well as a wide (200) reflection around 40°. A trace of metallic Ir is also present. This trace disappeared quickly upon cycling (see Figure A 9.3.5).

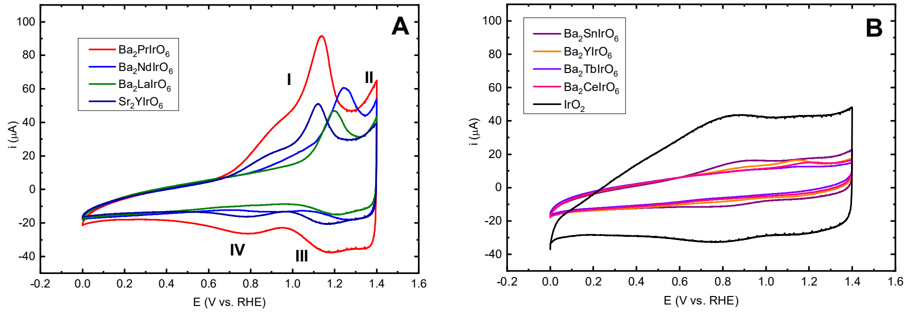

Figure 3.2: Voltammetric characterization of the Ir-based double perovskites used in this study, in a 0.1 M $HClO_4$ solution, supported on GC. All materials were scanned at least 20 times in the range of 1.30 – 1.55 V at 1500 RPM prior to characterization. Catalysts are shown in groups with pronounced Ir redox transitions (A) and those with less obvious features, plus the IrO_2 reference (B). Scan rate: 50 mV s^{-1}.

For the RRDE measurements, ethanol suspensions of the fine powders were dropcasted directly onto polished GC substrates and dried, followed by submersion and electrochemical measurements. We avoided the use of binders such as Nafion,[153,163,164] since it was found that Nafion had a major depressing effect on CER selectivity, likely due to its permselective behavior for cations (see Figure A 9.3.3).[165] ICP-MS control experiments showed that Nafion slightly enhanced Ir dissolution in Ba_2PrIrO_6 during the electrocatalytic LSV (Table A 9.3.2). The S-number however decreased very similarly (-47% vs. -48%) under the effect of chloride. These results suggest that dissolution is much less strongly affected by chloride mass transport than the CER.

Figure 3.2 displays the voltammetric characterization of ~38 μg cm^{-2} formal catalyst mass loadings of the investigated double perovskites and IrO_2 in the potential window of 0 – 1.4 V. On the basis of the stability results (section 3.3.1), we expect transient dissolution in all double perovskites during the RRDE measurements. All characterizations in Figure 3.2 were therefore taken from electrodes that were scanned at least 20 times in the potential region 1.30 – 1.55 V in 0.1 M $HClO_4$ at a rotation rate of 1500 RPM, to ensure that the voltammograms correspond to the actual catalyst surfaces that were used for subsequent OER and CER catalysis. The plots cannot be ascribed to idealized double perovskite surface structures but should be considered as double perovskite-derived thin IrO_x films in varying states of amorphization.

On the basis of their voltammetric characterization, we divided the materials into two groups. First, we consider Ba_2PrIrO_6, Ba_2NdIrO_6, Ba_2LaIrO_6 and Sr_2YIrO_6, which show strong redox transitions in the range of 0.6 – 1.4 V (Figure 3.2A). These transitions are tentatively ascribed to Ir redox transitions, as was done previously for Ba_2PrIrO_6.[154] Ba_2PrIrO_6 and Sr_2YIrO_6 show two sets of peaks in the forward scan (marked I and II) and in the backward scan (marked III and IV). Considering the position and irreversibility of the peaks, we ascribe these peaks to the formation of an amorphous IrO_x surface layer as a result of the leaching of A and B cations. Peaks I and IV likely correspond to a transition between Ir^{3+} and Ir^{4+}, whereas peaks II and III represent further Ir oxidation that may be beneficial for OER catalysis (either formation of Ir^{5+} centers,[166–168] or the more recently proposed formation of Ir^{4+}-O^{-}-moieties).[169,170] Second, the group of Ba_2SnIrO_6, Ba_2YIrO_6, Ba_2TbIrO_6 and Ba_2CeIrO_6 shows more subtle features (Figure 3.2B). It is somewhat surprising that Ba_2YIrO_6 and Ba_2CeIrO_6 do not have pronounced Ir redox peaks, since they also displayed significant dissolution upon contact in ICP-MS measurements (Table A 9.3.2). Possibly, an amorphous IrO_x layer is formed not during contact dissolution, but during potential scanning in the OER region. The rate of Ir dissolution during this scanning, which differs between catalysts, perhaps controls the extent to which the layer forms. The IrO_2 reference shows a broad profile with small reversible peaks around 0.8 V and 1.2 V, in accordance with previous studies on IrO_2.[150] We observed a trace of hydrogen evolution near 0 V for 'pristine' IrO_2 before scanning repeatedly into the OER, which we ascribe to a small amount of metallic Ir present in the bulk (see also Figure A 9.3.5). This behavior is no longer visible in Figure 3.2B because of the irreversible conversion of interfacial metallic Ir into its oxide, which is a much worse HER electrocatalyst.[171] See Figure A 9.3.5 for comparisons of the curves in Figure 3.2 with the catalysts in their 'pristine' state.

We must note that, in the context of this thesis, the focus is on selectivity and OER/CER interdependence, meaning we are not interested in absolute activities per se. It is however still desirable to apply normalization of current vs. the catalytically active surface area to allow comparison between different catalysts, even though the 'active site' could become ambiguous in the case of two distinct reactions. The most common and straightforward approach is normalization vs. the electrochemically active surface area (ECSA) by measuring the double layer capacitance $(C_{dl})_E$ around potential E, which is expected to scale with the ECSA according to:

$$\mathrm{ECSA} = \frac{(C_{dl})_E}{C_{dl}^*} \qquad \text{Eq. 3.1}$$

where C_{dl}^* is the specific capacitance per surface area of the material. $(C_{dl})_E$ can be determined from the slope of the double layer charging current vs. the scan rate (Figure A 9.3.7). Unfortunately, accurate ECSA determination is a persistent problem throughout electrocatalysis,[172] for four main reasons: i) accurate values of C_{dl}^* generally do not exist, ii) $(C_{dl})_E$ has to be measured in a region completely free of faradaic processes, iii) $(C_{dl})_E$ may be affected by the (potential-dependent) conductivity of the material, iv) determination of $(C_{dl})_E$ is not a selective chemical surface titration method, so that its value may actually not be the best measure of the ECSA.

Ideally, $(C_{dl})_E$ should be measured at the same potential for all materials. Considering Figure 3.2, there is large variation in behaviors for the studied materials within the potential window of 0 – 1.4 V. The Ir-related redox transitions in Figure 3.2A are visible in a wide potential range up until the OER/CER onset, which means that any $(C_{dl})_E$ measurement in this potential range is distorted by pseudo-capacitive contributions. McCrory *et al.* recommend measuring C_{dl} around the open circuit potential, but almost all measured materials assumed an open-circuit potential value that fell in the pseudo-capacitance area. In fact, the E_{OCP} value is likely not suitable in this regard, since it almost invariably depends on mixed potentials, i.e. the occurrence of multiple surface reactions resulting in zero net current. Other authors recommend electrochemical impedance modelling to measure the adsorption capacitance of reaction intermediates as an estimate of the ESCA.[173] In the end, we resorted to measuring $(C_{dl})_E$ in a 0.1 V interval centred around 0.1 V, hereby termed $(C_{dl})_{0.1\,V}$. This area appeared free of pseudo-capacitive processes for all materials (Figure 3.2). Assuming a specific capacitance $C_{dl}^* = 0.059\ \mathrm{mF\ cm^{-2}}$, an 'average' of reported literature values for oxides in acidic conditions,[66,153] we obtained ECSAs with similar magnitudes as the geometrical surface area. The caveat of this method is the large separation of OER-relevant potentials and the ECSA determination. Under the assumption that the Ir centers dictate the observed pseudo-capacitive behavior, we also cannot exclude interference from conductivity (category iii), since amorphous Ir oxides show a notable decrease of conductivity below 0.5 V.[174] In effect, this means that part of $(C_{dl})_{0.1\,V}$ may originate from the GC substrate.[175,176] Despite the shortcomings of this normalization method, it has to be noted again that the activity normalization affects neither the slope of Tafel curves, the reaction order analysis, or OER vs. CER selectivity.

3.3.3. OER and CER activity trends

In consideration of section 3.3.1 and 3.3.2, we will not theorize about catalyst structure vs. catalytic activity relationships, since the true structure of the double perovskite surfaces is not known. The materials show rather diverse catalytic behavior as will be shown below.

In the following sections, the RRDE method described in Chapter 2 will be implemented to measure individual OER and CER current densities. As discussed in that chapter, the total current on the disk electrode (i_D) is assumed to be the sum of CER current (i_{CER}), OER current (i_{OER}), and a residual current originating from scanning (pseudo)capacitance. The capacitive contribution was effectively minimized by using a relatively slow scan rate of 10 mV s^{-1} and averaging forward and backward scans, yielding approximately only catalytic current from the catalytic OER and CER, which are solution-controlled processes. Values of i_{CER} were again obtained by correcting the ring currents (i_R) for the collection factor of chlorine, which had a value of $N_{Cl_2} \approx 0.215$ in 0.1 M $HClO_4$. The remaining current on the disk was then assumed to originate from the OER. See Figure A 9.3.6 for an example curve measured during a typical experiment.

Due to the perceived instability of the catalysts under study, we must note that the ring measurements may be affected by dissolved species coming from the disk. These species could cause additional stray reduction reactions, or interfere with Cl_2 detection by re-depositing as species which are not active towards Cl_2 reduction. As evidenced by their Pourbaix diagrams,[177] most A and B cations used in this study are expected to be electrochemically inert at 0.95 V in acidic solution, meaning they will not react or deposit on the Pt ring. Only Sn and solution-phase Ir species may possibly deposit as oxides under the studied conditions. From the Ir dissolution rates in ICP-MS measurements, we estimate that the error due to reduction reactions involving Ir is at least two orders of magnitude lower than the smallest ring currents related to CER (Figure A 9.3.4). Furthermore, a rough estimate shows that it would take at least 10 minutes of continuous operation at high potential to form a perfect IrO_2 monolayer on

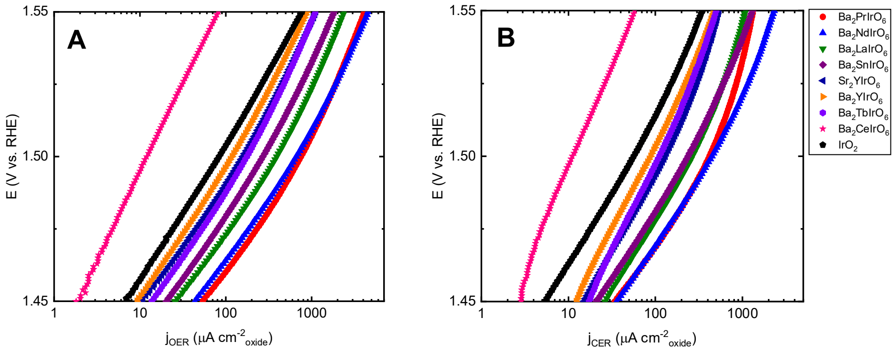

Figure 3.3: OER (A) and CER (B) Tafel curves obtained by scanning the electrode between 1.30 and 1.55 V at 10 mV s^{-1}. A: 'pure' OER current densities in a 0.1 M $HClO_4$ solution. B: CER current densities in a 0.1 M $HClO_4$ + 20 mM NaCl solution, derived from ring currents on a Pt ring fixed at 0.95 V vs. RHE. Values shown are the average of at least three independent measurements (see Figure A 9.3.9 for a version containing error bars). Solutions saturated with Ar, rotation rate 1500 RPM.

the ring. Serious interference at the Pt ring can thus be safely excluded (see section 9.3.1 for full details).

The value of the Tafel slope has been used as a ‘benchmark’ for catalytic OER performance, with a lower Tafel slope correlating with a ‘better catalyst’.[178–180] It must be noted that strictly speaking, the catalytic performance of a material is not governed by the Tafel slope only. A low Tafel slope is only favorable if it leads to a low(er) overpotential at the desired current density. The experimental findings related to the Tafel slope are discussed in this spirit; namely, that catalytic performance and the Tafel slope are not by definition correlated.

Initially, ‘pure OER’ currents (in absence of Cl^-), as well as CER currents were measured during the parallel evolution of oxygen and chlorine. Figure 3.3A shows OER Tafel plots constructed from capacitance-corrected disk current densities, in absence of Cl^-. Figure 3.3B shows CER Tafel plots constructed from ring currents in presence of 20 mM Cl^-. The activities for the OER roughly follow the order Pr ≈ Nd > La > Sn > Sr_2Y ≈ Tb > Ba_2Y > IrO_2 > Ce. The most catalytically active DPs Ba_2PrIrO_6, Ba_2NdIrO_6, Ba_2LaIrO_6 and Sr_2YIrO_6, also show a redox transition in their blank CVs (see Figure 3.2A). We speculate that activities correlate to the extent of surface leaching, although a definite correlation between activity and total dissolved

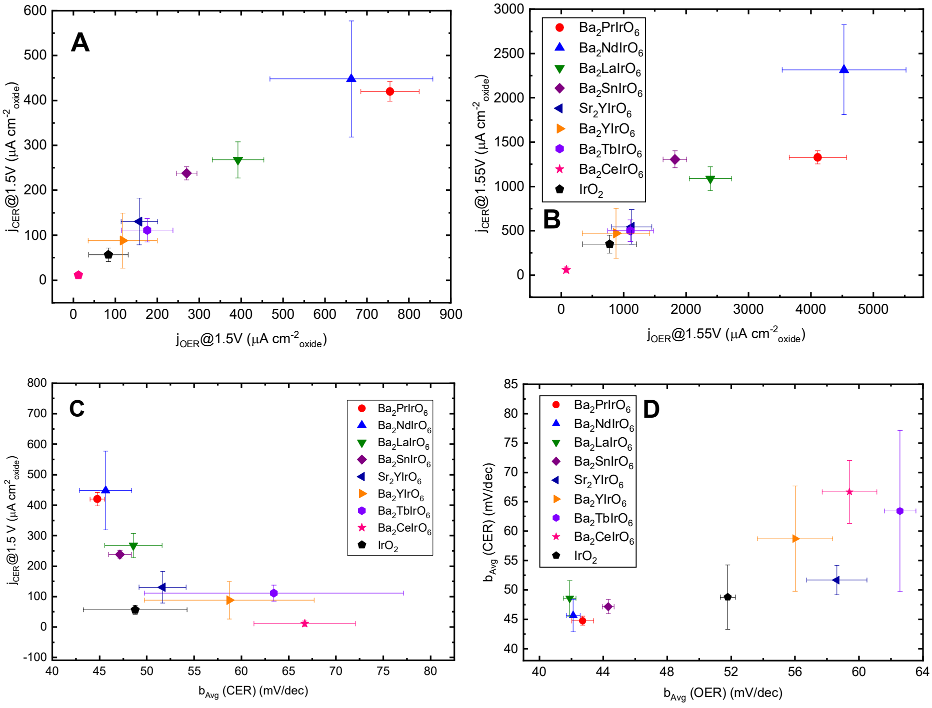

Figure 3.4: Correlations between OER and CER activities, data derived from Figure 3.3 (CER measured in 20 mM NaCl). A and B: OER vs. CER current densities compared at 1.50 V and 1.55 V, respectively. C: Comparison of CER Tafel slope vs. current densities measured at 1.50 V, the upper potential limit of the linear portion. D: Comparison of Tafel slopes from linear portions (1.45-1.50 V) of the OER and CER. All data are averages of at least three independent measurements. Error bars represent corresponding standard deviations.

amounts could not be established (see sections 3.3.1 and 3.3.2). Interestingly, the same order in activity is observed for the CER, indicating scaling between OER and CER activities. To minimize mass transport control in case of CER, the experiments were performed at 1500 RPM. The highest measured CER current densities per geometric area, as measured at 1.55 V on Ba_2PrIrO_6, were approximately 10% of the theoretical diffusion limited current as predicted by the Levich equation. Therefore, it can be assumed that mass transport effects on CER are negligible in the potential ranges studied. The OER is considered effectively immune to mass transport effects.

Figure 3.4A and B show a comparison of CER and OER current densities for all materials, plotted at 1.50 V and 1.55 V. As already faintly visible from Figure 3.3, there is a linear scaling relationship between OER and CER activity. Although such a relationship has been observed in previous literature, it must be noted that this is one of the few reports directly showing a correlation between CER and OER activity among a group of catalysts.[55] Furthermore, all materials, including the least active ones, showed regions of linear Tafel phenomena for both the OER and CER ($R^2 > 0.98$). The slopes of these linear CER Tafel sections are shown in Figure 3.4C, in comparison to CER current densities at 1.50 V. A lower Tafel slope generally correlates with higher CER current densities, which is a reasonable finding due to the exponential nature of the j/E curves. Furthermore, the catalytically most active materials display linear Tafel slopes in the range 45-50 mV/dec for the CER, and slopes of 40-45 mV/dec for the OER (D). For the less active materials, higher Tafel slopes with a higher variance are observed (see Table A 9.3.3 for all numerical Tafel slope values).

Considering the instability of the materials, we must comment on the possible origin of the linear relation between OER and CER activity. As previously mentioned, the selective leaching of non-noble A and B cations from the lattice will to a varying extent form an amorphous IrO_x surface layer on all materials. Since the double perovskites share identical structural motifs,

one can expect them to follow comparable amorphization behavior. This could result in thin catalytically active IrO_x layers with perhaps varying surface area but similar kinetics, and thus a linear OER vs. CER relation would always be observed. However, the variance in Tafel slopes for the CER strongly speaks against this effect being the only descriptor for the OER and CER activity;[56,181] if identical IrO_x is formed, then all semi-logarithmic i-E curves should display nearly identical (±5 mV/dec) Tafel slopes, which is not the case. The IrO_2 reference furthermore fits in the scaling trend very well, despite possessing a rather different structure compared to the double perovskites. All in all, although the true nature and structure of the active catalyst phases cannot be discerned, we can still conclude that they vary among catalysts, and that despite this, a linear scaling relationship between the CER and OER is observed. The origin of this scaling has been commented on by Trasatti.[55] It is possibly a similarity between the way that chloride binds to surfaces, as compared to the several key oxygen intermediates believed to be involved in the OER.[72] Most importantly, scaling suggests that a catalyst with a kinetic preference towards only one of the reactions may be very hard to find.

CER selectivity as a function of chloride concentration

Similar to Chapter 2, we further probed the OER vs. CER selectivity of the materials by varying the chloride concentration stepwise between 0 and 120 mM. Molar selectivities towards CER (ε_{CER}) were defined according to Eq. 2.3. Measured values of ε_{CER} for all materials are shown in Figure 3.5, at 1.50 V and 1.55 V. At 1.50 V, ε_{CER} is very similar among materials and shows a strong dependence on chloride concentration. At 1.55 V (Figure 3.5B), selectivity towards the OER increases and there is more variance among materials. A group consisting of Ba_2PrIrO_6, Ba_2NdIrO_6, Ba_2LaIrO_6 and Sr_2YIrO_6 shows particularly high OER selectivity. At both potentials shown, the least active materials generally show higher selectivity towards CER. An important exception is Ba_2SnIrO_6. This material shows relatively high CER selectivity at both 1.50 V and 1.55 V while also possessing relatively high activity.

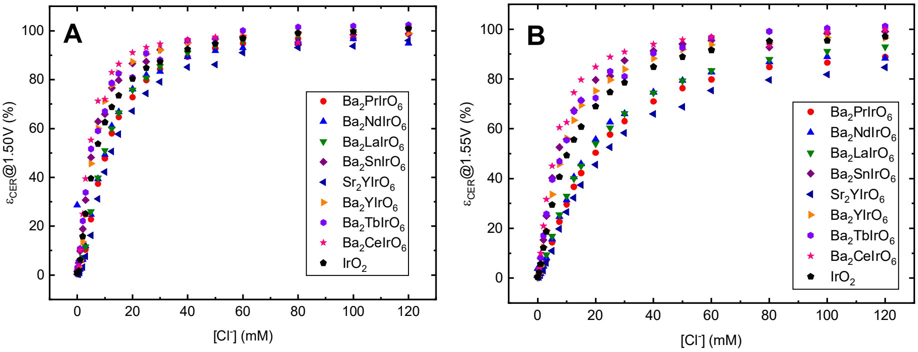

Figure 3.5: CER selectivity (ε_{CER}, definition in main text) as a function of $[Cl^-]$, for different Ir double perovskites and the IrO_2 reference. Values shown at 1.50 V (A) and 1.55 V (B). Values were obtained with the RRDE method as described in section 3.3.3.

Despite these differences, it can be said that ε_{CER} is globally governed by a single relationship none of the materials show extremely diverging values (>20%) in their selectivity between the OER and CER. This conclusion is in-line with Figure 3.4A and Figure 3.4B, where a scaling trend was seen at the single concentration $[Cl^-]$ = 20 mM. This tendency seems to be applicable to higher chloride concentrations as well. The effect of mass transport on the measured CER currents should not be high. A 10% decrease in CER current, the prediction for maximum mass transport control in the experiments (see also the discussion of Figure 3.3), should lead to a decrease in ε_{CER} of less than 2% for virtually all chloride concentrations. At potentials above 1.55 V, selectivity towards the OER will presumably increase, since CER will become increasingly mass transport limited whereas the OER is much less affected. Unfortunately it was not possible to probe this potential region due to formation of persistent O_2 bubbles at high current densities on the electrode tip, which interfered with the collection efficiency. See Chapter 8 for a deeper discussion of this problem.

3.3.4. <u>OER vs. CER interdependence and effect of chloride concentration</u>

In this section, we look more deeply into the parallel evolution of oxygen and chlorine as a function of chloride concentration. Figure 3.6 shows the effect of chloride regarding the OER Tafel curves, as well as relative OER and CER activity. The chloride concentration exhibits a pronounced influence on all catalysts under study regarding both the CER and OER. When comparing Figure 3.6A to Figure 3.3A, the presence of 20 mM Cl^- induces a shift of the OER Tafel curves towards higher potentials, a reduction in the apparent OER exchange current density and thus a decrease in the OER activity (a factor of 2 for most materials). A scaling relationship was again apparent when OER data from Figure 3.6A was compared to CER data from Figure 3.3B (see Figure A 9.3.10). Figure 3.6B and Figure 3.6C show relative OER and CER currents as a function of increasing $[Cl^-]$. For the OER, all values are shown as percentages relative to the value at chloride free conditions ($[Cl^-]$ = 0 mM). Likewise, all values for the CER are shown relative to $[Cl^-]$ = 30 mM, where the value of the current at this concentration was taken as '30%'. This normalization was done due to the different current densities, and allows a clearer comparison between trends among materials as chloride concentrations increase (see Figure A 9.3.12 for the absolute currents). Figure 3.6B shows a

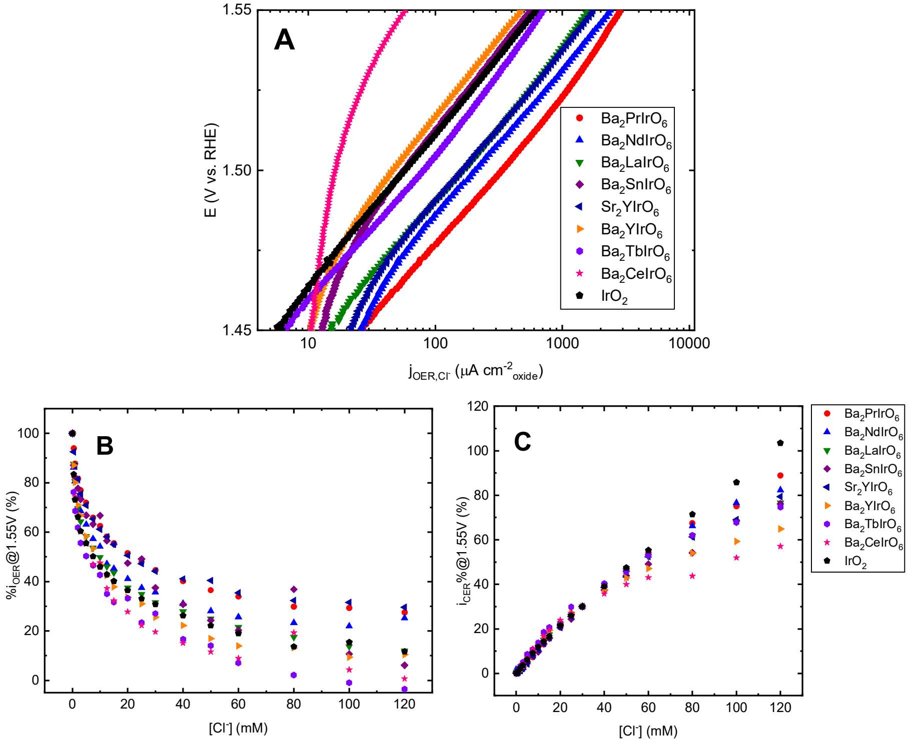

Figure 3.6: Effect of chloride concentration on the OER and CER. A: OER currents measured in the presence of 20 mM NaCl, in parallel with CER. B and C: Relative OER current (B) and CER current (C) as function of increasing chloride concentration. %OER currents shown relative to chloride free conditions (0 mM NaCl), %CER currents shown relative to 30 mM NaCl. See Figure A 9.3.12 for versions of A and B containing absolute currents.

nonlinear decrease in OER current as a function of $[\mathrm{Cl}^-]$ on all materials, in some cases (Ba_2TbIrO_6 and Ba_2CeIrO_6) approaching virtually complete OER suppression at 120 mM. At the same time, all materials show a continuous CER increase with increasing $[\mathrm{Cl}^-]$ (Figure 3.6C), but there is significant downward curvature in all plots except for the IrO_2 reference.

For further analysis of the interdependence between the OER and CER, we consider a model for the apparent suppressing effect of Cl^- on the OER activity. The simplest approach to explain this phenomenon would be to assume a simple site blocking, similar to previous work by Fernández and co-workers:[182]

$$i_{OER} = i_{OER}^{0}(1-\theta_{Cl}) = i_{OER}^{0}\left(1-\frac{K_{Cl}[\mathrm{Cl}^-]e^{f\eta}}{1+K_{Cl}[\mathrm{Cl}^-]e^{f\eta}}\right) \qquad \text{Eq. 3.2}$$

In this equation, i_{OER} describes the measured OER current; i_{OER}^{0} describes the OER current that would have been measured in absence of chloride. The other symbols again relate to a Volmer-type adsorption of chloride in pseudo-equilibrium. The corresponding OER chloride reaction order dependence then becomes:

$$\mathcal{R}_{\mathrm{Cl}^-}^{\mathrm{OER}} = \left(\frac{\partial \ln i_{OER}}{\partial \ln[\mathrm{Cl}^-]}\right)_E = -\frac{K_{Cl}[\mathrm{Cl}^-]e^{f\eta}}{1+K_{Cl}[\mathrm{Cl}^-]e^{f\eta}} \qquad \text{Eq. 3.3}$$

From this expression, we expect $\mathcal{R}_{\mathrm{Cl}^-}^{\mathrm{OER}}$ to change from 0 to -1 as $[\mathrm{Cl}^-]$ increases, the rate of change depending on the overpotential and K_{Cl}. We will also consider the chloride reaction orders of the CER ($\mathcal{R}_{\mathrm{Cl}^-}^{\mathrm{CER}}$), and compare them with predictions from microkinetic models described in section 1.4.

The experimental OER and CER reaction orders can be approximated from the derivative of log-log plots (see Figure A 9.3.15) of the i vs. $[\mathrm{Cl}^-]$ curves. The results are shown in Figure 3.7. Reaction orders for the OER and CER that were measured on IrO_x/GC in Chapter 2 (section 2.3.4) have been included for comparison. As described in 2.3.3, the results for values of $[\mathrm{Cl}^-]$ < 10 mM in Figure 3.7 may not be fully reliable due to possible interference of oxide formation on the Pt ring used for detection.

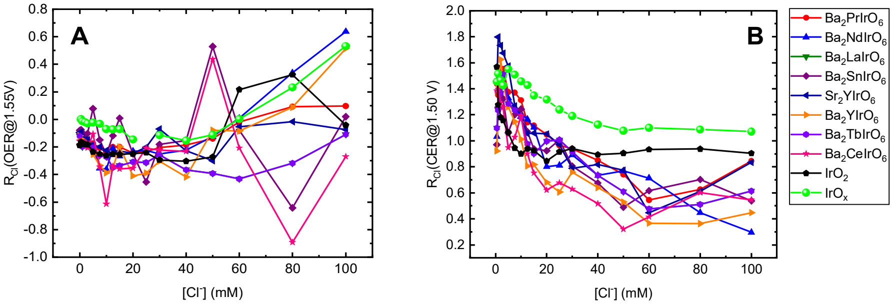

Figure 3.7: Reaction orders vs. chloride concentration ($\mathcal{R}_{Cl^-}$) for the OER (A) and CER (B). Values were derived using the $[Cl^-]$-dependent slopes of Figure A 9.3.15.

The initial focus of the discussion will lie on the OER chloride reaction order, for $[\mathrm{Cl^-}]$ concentrations of up to 50 mM (see Figure A 9.3.16 for a close-up of this region). In this range, $\mathcal{R}_{\mathrm{Cl^-}}^{\mathrm{OER}}$ has a negative fractional value between -0.2 and -0.4 for all materials tested in this study, as was already apparent from the continuous decrease in OER activity in Figure 3.6B. Interestingly, the previously characterized $\mathrm{IrO_x}$ has a value of $\mathcal{R}_{\mathrm{Cl^-}}^{\mathrm{OER}}$ closest to 0, varying between 0 and -0.1. This is illustrative of this material's OER kinetics being almost impervious to the presence of chloride or parallel chlorine evolution, in contrast with the double perovskites. For these materials, $\mathcal{R}_{\mathrm{Cl^-}}^{\mathrm{OER}}$ is generally less negative the higher the intrinsic activity of the material, except for the $\mathrm{IrO_2}$ reference, which shows relatively low activity but globally also one of the least negative values of $\mathcal{R}_{\mathrm{Cl^-}}^{\mathrm{OER}}$. Furthermore, most OER Tafel curves exhibit negligible changes in slope after the addition of $\mathrm{Cl^-}$, except for $\mathrm{Ba_2CeIrO_6}$ (see Figure A 9.3.11 for a comparison and Table A 9.3.3 for the full data). This suggests that $\mathrm{Cl^-}$ does not change the OER mechanism, which (along with the decreasing fractional reaction order in Figure 3.7A) is in agreement with the simple site blocking model. However, the extent of blocking appears to depend sensitively on the type of material. We hypothesize that site blocking for a more amorphous catalyst is different from that in a less amorphous system. The OER data at $[\mathrm{Cl^-}]$ exceeding 50 mM are subject to increasing levels of uncertainty, due to inherent limitations of the experiment. With rising chloride concentration, the CER contribution starts to dominate the OER current, as a result of which the experimental noise is greatly amplified in subtle slope changes of the log-log plots. Extensive averaging or smoothing may alleviate the noise, but we chose to present the data as-is to illustrate limitations of the method. Despite the noise, the overall trend nonetheless suggests that the reaction order never reaches -1, but rather seems to increase again, occasionally reaching positive values. This may reflect the influence of chloride on the actual structure of the catalytic interface.

Regarding the CER in Figure 3.7B, $\mathcal{R}_{\mathrm{Cl^-}}^{\mathrm{CER}}$ also decreases continuously for all double perovskites, down to values of roughly 0.5. For $\mathrm{IrO_2}$ however, it stays at a constant value close to unity, $\mathcal{R}_{\mathrm{Cl^-}}^{\mathrm{CER}} \approx 0.92$. The $\mathrm{IrO_x}$ reference material shows even different values, with $\mathcal{R}_{\mathrm{Cl^-}}^{\mathrm{CER}} \approx 1.45$ around $[\mathrm{Cl^-}]$ = 10 mM, which then progressively decreases to a steady value of 1.07. A $\mathcal{R}_{\mathrm{Cl^-}}^{\mathrm{CER}}$ value close to one has often been reported on metal oxides.[35,55,112,183,184] Furthermore, a decrease in $\mathcal{R}_{\mathrm{Cl^-}}^{\mathrm{CER}}$ as a result of an increase in $[\mathrm{Cl^-}]$ has been reported previously on $\mathrm{RuO_2}$.[185] Judging from reaction orders alone, it thus seems likely that both $\mathrm{IrO_x}$ and $\mathrm{IrO_2}$ follow a Volmer-Heyrovský mechanism, as their reaction orders converge near 1 at higher $[\mathrm{Cl^-}]$. This is in agreement with previous reports.[35] On the other hand, reaction orders on all double perovskites continuously decrease to values much lower than 1. Such behavior is more expected of either a Volmer-Tafel or Volmer-Krishtalik mechanism dominating the kinetics. We further investigated the CER mechanism using test plots devised by Conway *et al.*[118] and Ferro *et al.*[113] By re-ordering the measured CER i-E curves, one can test whether a Volmer-Tafel or Volmer-Heyrovský mechanism applies (see Figure A 9.3.13 and its description for details about the method). For $\mathrm{IrO_2}$, we obtained a straight line in a Ferro-de Battisti test plot only, indicating Volmer-Heyrovský kinetics. We note that a straight line in such a plot can also indicate Volmer-Krishtalik kinetics. However, the y-intercept is then expected to be independent of $[\mathrm{Cl^-}]$. Instead, the intercept shows an inverse $[\mathrm{Cl^-}]$ dependence, which matches well with the V-H pathway (see Figure A 9.3.14 for more details). On the other hand, Ba_2PrIrO_6 only showed a straight line in a Conway-Novák test plot, suggesting that CER proceeds via a Volmer-Tafel mechanism on this material (and perhaps also on the other perovskites), in agreement with the reaction order findings.

As a final note, it can be expected that the apparent OER and CER chloride reaction orders on the double perovskites are affected by adventitious surface leaching as described in section 3.3.1. This leaching should lead to transient changes of the active surface area, and its effect on either $\mathcal{R}_{Cl^-}^{OER}$ or $\mathcal{R}_{Cl^-}^{CER}$ can be modelled via:

$$i = A([\mathrm{Cl}^-])j \qquad \text{Eq. 3.4}$$

where i is the measured current for either the OER or CER, j is the current density as modelled by either the V-T or V-H model, and A is the real electrochemical surface area, which is dependent on chloride concentration due to leaching. It then follows that:

$$\mathcal{R}_{\mathrm{Cl}^-} = \left(\frac{\partial \ln i}{\partial \ln[\mathrm{Cl}^-]}\right)_E = \frac{\partial \ln j}{\partial \ln[\mathrm{Cl}^-]} + \frac{\partial \ln A([\mathrm{Cl}^-])}{\partial \ln[\mathrm{Cl}^-]} \qquad \text{Eq. 3.5}$$

On the right-hand side, the first term corresponds to the 'kinetic' reaction order, as discussed earlier in this section. The second term represents the influence of chloride on the real surface area. As seen in Figure 3.1 and Table A 9.3.2, the leaching rates of both noble and non-noble components are chloride-dependent, but not in the same manner; a complex interplay can be expected from surface area changes due to increasing chloride concentration. Not much is currently known on the growth of amorphous surface phases on these materials in acidic media, meaning that the value and range of the A term is not easy to quantify. A reasonable assumption is that the term $\partial \ln A([\mathrm{Cl}^-]) / \partial \ln[\mathrm{Cl}^-]$ is positive immediately upon contacting the pristine perovskite with acidic electrolyte, during which the majority of surface leaching takes place and the change in surface area should be the largest. Considering that the rate of leaching steadily decreases over time in Figure 3.1, we may expect A to approach a constant value for all values of $[\mathrm{Cl}^-]$, and its contribution to the reaction order should then tend to 0. On the other hand, if the rate of leaching increases strongly with increasing $[\mathrm{Cl}^-]$, increasing changes of A could explain the apparent rise in reaction orders for both the OER and CER at higher Cl^- concentrations.

3.4. Conclusions

In this chapter, we report that iridium-based double perovskites with structures Ba_2BIrO_6 (B = Pr, Nd, La, Sn, Y, Tb, Ce) and Sr_2YIrO_6, previously reported having high oxygen evolution activity in acidic media, also show high catalytic activity towards chlorine evolution in relatively low chloride concentrations (0 – 120 mM). A strong linear correlation between the CER and OER activity was found on all catalysts employed, and also comparable selectivity. This strengthens the suggestion that the OER and CER follow a scaling relationship, as suggested in previous studies. On the basis of these results, it can be expected that promoting one reaction over the other on the basis of kinetic considerations alone may be exceedingly difficult, if not impossible. Alternative pathways, such as affecting the CER thermodynamics through pH changes, or the mass transport of chloride to the active catalyst, are likely more successful in enhancing selectivity. Electrochemical ICP-MS measurements showed that chloride has mixed effects on the stability of the perovskites. Whereas non-noble dissolution effects were inconclusive, it significantly enhanced iridium dissolution during potentiodynamic control and active OER/CER, as evidenced by a lower value of the *S*-number. Dissolution pathways related to the OER and CER are therefore likely different, which must be taken into account when considering an active catalyst for either of the reactions. Reaction order analysis indicates that CER proceeds via Volmer-Tafel mechanism on the double perovskites, whereas it follows a Volmer-Heyrovský mechanism on IrO_2 and amorphous IrO_x. Contrary to amorphous IrO_x, the OER activity on the double perovskites and IrO_2 is strongly impacted by chloride concentration, displaying fractional, negative reaction orders.